

Oxygen exchange materials for solar thermochemical splitting of H₂O and CO₂

A review

Journal Article**Author(s):**

Scheffe, Jonathan R.; [Steinfeld, Aldo](#) 

Publication date:

2014-09

Permanent link:

<https://doi.org/https://doi.org/10.3929/ethz-b-000089758>

Rights / license:

[Creative Commons Attribution-NonCommercial-NoDerivatives 4.0 International](#)

Originally published in:

Materials Today 17(7), <https://doi.org/10.1016/j.mattod.2014.04.025>

Funding acknowledgement:

- Solar thermochemical production of fuels ()



Oxygen exchange materials for solar thermochemical splitting of H₂O and CO₂: a review

Jonathan R. Scheffe^{1,*} and Aldo Steinfeld^{1,2}

¹Department of Mechanical and Process Engineering, ETH Zurich, 8092 Zurich, Switzerland

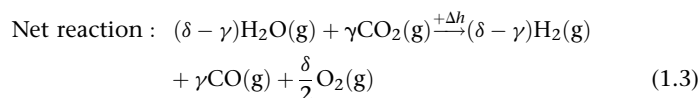
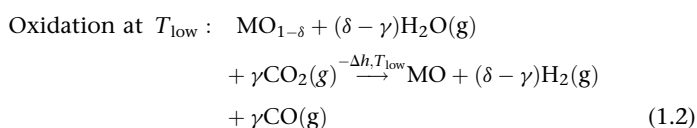
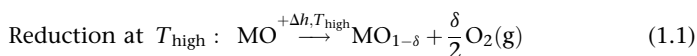
²Solar Technology Laboratory, Paul Scherrer Institute, 5232 Villigen PSI, Switzerland

This review summarizes state of the art metal oxide materials used in two-step thermochemical redox cycles for the production of H₂ and CO from H₂O and CO₂ using concentrated solar energy. Advantages and disadvantages of both stoichiometric (e.g. iron oxide based cycles) and nonstoichiometric (e.g. ceria based cycles) materials are discussed in the context of thermodynamics, chemical kinetics, and material stability. Finally, a perspective aimed at future materials development and requirements necessary for advances of process efficiencies is discussed.

Introduction

Conversion of abundant but intermittent solar energy to fungible liquid hydrocarbon fuels can potentially provide a seamless transition for the integration of renewable fuel sources in the existing transportation infrastructure. There are numerous pathways to convert sunlight to chemical intermediates, including photochemical, electrochemical, thermochemical and their combinations. In particular, thermochemical processes using concentrated solar energy offer the potential to achieve high solar-to-fuel energy conversion efficiencies ($\eta_{\text{solar-to-fuel}}$, defined as the ratio of heating value of the fuel to the solar energy input) [1]. This is primarily related to the fact that solar thermal processes inherently operate at high temperatures and utilize the entire solar spectrum, and as such provide a thermodynamically favorable path to solar fuels production.

Solar thermochemical redox cycles most commonly operate in two separate reduction/oxidation steps utilizing a metal oxide (MO) as a reactive intermediate:



In the first step the metal oxide is reduced at elevated temperatures (generally $T_{\text{high}} > 1473$ K) driven by concentrated solar energy (q_{solar}). In the second step, the reduced oxide is reacted with H₂O and CO₂ at temperatures $T_{\text{low}} \leq T_{\text{high}}$ to produce H₂(g) and CO(g). The resulting synthesis gas mixture can be catalytically converted to fungible liquid hydrocarbon fuels (gasoline, diesel, kerosene, etc.) through industrially proven technologies such as Fischer–Tropsch synthesis [2]. The deviation from stoichiometry, δ , otherwise known as the oxygen storage capacity, is directly related to the maximum amount of fuel capable of being produced. Thus, process efficiencies are directly related to a materials oxygen storage capacity ($\eta_{\text{solar-to-fuel}} \propto \delta/q_{\text{solar}}$). Because the metal oxide is recycled, the net reactions are simply H₂O(g) → H₂(g) + O₂(g) and CO₂(g) → CO(g) + O₂(g). In contrast to direct thermolysis, reactions occur at considerably lower temperatures [3,4] (i.e. $\Delta G_{\text{H}_2\text{O}(\text{g}) \rightarrow \text{H}_2(\text{g}) + \text{O}_2(\text{g})} = 0$ at $T = 4100$ K [5]) and the need for high-temperature separation of the fuel and O₂ are eliminated. Thorough reviews of thermochemical cycles that discuss reactor considerations, theoretical efficiencies of different redox pairs, and economics have been performed by Steinfeld et al. [6,7], Kodama and Gokon [8] and the U.S. Department of Energy [9]. Here we focus specifically on reviewing state of the art metal oxide redox

*Corresponding author: Scheffe, J.R. (jscheffe@ethz.ch)

pairs utilized within solar thermochemical reactors, compare and contrast their physical properties (kinetics, thermodynamics, etc.) and discuss how their properties affect operational strategies.

Metal oxide redox pairs

Over 350 thermochemical redox cycles are known to be thermodynamically capable of dissociating H₂O to produce H₂, many of which have theoretical efficiencies of over 40% [10]. Of these potential cycles, only a minority operate in two discreet steps according to Eqns. (1.1) and (1.2), while the remainders occur in 3 or more steps. In general, two step cycles can be divided into two categories; volatile and non-volatile. Non-volatile cycles utilize metal oxides which remain in the solid state during reduction (i.e. Fe₃O₄(s) → FeO–Fe₃O₄(s) [4]), while volatile redox cycles consist of metal oxides that undergo gas–solid phase transitions (i.e. ZnO(s) → Zn(g) [11]). In general, volatile reactions have a greater oxygen exchange capability than non-volatile reactions (more O₂ release/uptake, and thus fuel production, per mass of oxide) and reduction is thermodynamically more favorable due to the increased entropy generated resulting from gas phase products. Nevertheless, the volatile products must be quenched rapidly to avoid recombination, and to date this issue has not been solved in an energetically efficient fashion [12].

Non-volatile metal oxides cycles can be further categorized into two subcategories, namely stoichiometric and non-stoichiometric cycles. Stoichiometric reactions generally form solid solutions upon reduction (i.e. Fe₃O₄(s) → FeO–Fe₃O₄(s) [4]) and Fe³⁺ is partially reduced to Fe²⁺. Non-stoichiometric oxides remain crystallographically stable while the lattice accommodates changes in anion or cation vacancies concentrations (i.e. CeO₂(s) → CeO_{2–δ}(s) [13]). For both stoichiometric and non-stoichiometric cycles, doping or substitution strategies are often employed to affect their thermodynamic, kinetic and physical properties. For example, doping ceria with Zr⁴⁺ is known to increase its oxygen storage capacity due to its ability to destabilize the fluorite lattice [14]. In general, stoichiometric reactions have a greater oxygen storage capacity than non-stoichiometric reactions, but are hindered by slower reaction kinetics (controlled by either bulk solid state diffusion or surface reactions) and poor stability (either chemical or morphological), properties which are practically related to $\eta_{\text{solar-to-fuel}}$ because they are directly tied to the specific reactor design chosen. This in turn dictates how efficiently radiation and reactive gases are transferred to the material. A current summary of the most commonly investigated two-step oxide pairs, their simplified reaction schemes, and exemplary references are described in Table 1.

Iron oxide

The first two step cycle was proposed by Nakamura [4] using Fe₃O₄/FeO as a redox pair. Originally proposed to operate at temperatures as high as 2500 K (Fe₃O₄ $\xrightleftharpoons[T=2500\text{ K}]{\Delta G=0}$ 3FeO + (1/2)O₂), this cycle is complicated by melting of Fe₃O₄ which occurs at temperatures greater than 2000 K, and the product wustite which melts at temperatures as low as 1643 K [4,35]. Practically, this reaction can be driven at lower temperatures by reducing the oxygen partial pressure (p_{O_2}). For example, from thermodynamic data of Bransky and Hed [36], Darken and Gurry [37], and Salmon [38], Fe_{0.95}O (further reduction extents infringe the Fe–wustite phase boundary) is thermodynamically favored at 1573 K and 1273 K at low oxygen partial pressures of 10^{–11} and 10^{–15} atm, respectively. While classified as stoichiometric, the wustite phase is stable over a range of stoichiometries, roughly between Fe_{0.95}O and Fe_{0.85}O, but its stability range increases with temperature [38]. For lower reduction extents intermediate mixed phases of FeO–Fe₃O₄ are thermodynamically predicted [39,40], while at very low reduction extents, magnetite is nonstoichiometric [41].

Cycle feasibility at reduced oxygen partial pressures with pure Fe₃O₄ has been experimentally demonstrated [19], but magnetite is often stabilized on, or dissolved in, inert materials such as YSZ and ZrO₂ [18,20,21] to suppress problems associated with melting and sintering. Kodama et al. have studied the reduction (1673 K) and oxidation (1273 K) of pure Fe₃O₄ compared to 20–25 wt% Fe₃O₄ mixed with 3YSZ and report two significant findings. Firstly, that pure magnetite was capable of being reduced at low oxygen partial pressures ($p_{\text{O}_2} \approx 10^{-7}$ bar), but in the process became dense, sintered and glossy, presumably due to the fact that operation was conducted above the melting point of the reduced wustite phase ($T_m = 1643$ K). Secondly, that when supported on YSZ, the reduced wustite phase (Fe²⁺) becomes dissolved in the YSZ lattice and thus melting is avoided. Upon oxidation with steam, the dissolved Fe²⁺ was capable of being re-oxidized to reform Fe₃O₄.

Coker et al. have further studied the Fe–8YSZ system and report that Fe²⁺ concentrations as high as 9.4 mol% are stable within the cubic lattice. Furthermore, they observed that dissolved iron is more redox active than undissolved, in agreement with Kodama et al. [20]. This was attributed to the fact that dissolved Fe²⁺ oxidation rates are limited by rapid oxygen diffusion through the YSZ lattice, whereas undissolved Fe²⁺ present within a magnetite–wustite solid solution is limited by the relatively slow Fe²⁺ diffusion. This hypothesis was confirmed with Time-of-Flight Secondary Ion Mass Spectrometry (ToF-SIMS) analysis using isotopically labeled C(¹⁸O)₂ as an oxidant

TABLE 1

Common two step redox pairs, their associated redox category, cycle name, reduction scheme and references.

| Category | Cycle name | Simplified reduction reaction | Ref. |
|----------------------------------|-------------|--|------------|
| Volatile | Zinc oxide | ZnO(s) → Zn(g) | [11,15,16] |
| | Tin oxide | SnO ₂ (s) → SnO(g) | [17] |
| Non-volatile (stoichiometric) | Iron Oxide | Fe ₃ O ₄ → FeO | [4,18–21] |
| | Ferrite | M _x Fe _{3–x} O ₄ → xMO + (3 – x)FeO | [22–24] |
| | Hercynite | Fe ₃ O ₄ + 3Al ₂ O ₃ → 3FeAl ₂ O ₄ | [25–27] |
| | | M _x Fe _{3–x} O ₄ + 3Al ₂ O ₃ → (3–x)FeAl ₂ O _{4–x} + xMAl ₂ O ₄ | |
| Non-volatile (nonstoichiometric) | Ceria | CeO ₂ → CeO _{2–δ} | [13,28,29] |
| | Doped ceria | M _x Ce _{1–x} O ₂ → M _x Ce _{1–x} O _{2–δ} | [30–32] |
| | Perovskite | ABO ₃ → ABO _{3–δ} | [33,34] |

[42]. $^{18}\text{O}/^{16}\text{O}$ ratios following oxidation of mostly dissolved Fe^{2+} were uniform throughout the sample, indicating complete oxygen exchange of released ^{16}O during thermal reduction with ^{18}O during oxidation. Samples with undissolved Fe^{2+} , on the other hand, show a noticeable decrease in the ^{18}O concentration within magnetite–wüstite grains, as seen in Fig. 1. Additionally, the effect is greater for larger grains (see particle 1 versus particle 2) and even after 7 h exposure to $\text{C}(^{18}\text{O})_2$, large gradients of $^{18}\text{O}/^{16}\text{O}$ still existed in all but the smallest iron oxide grains ($d_{\text{average}} = 18 \mu\text{m}$). This observation clearly shows that either exceptionally small length scales (i.e. aerosolized particles or engineered nanostructures [43]) or the presence of inert diluents are required for this cycle to be feasible from a kinetic perspective. However, because of sintering and melting concerns, such small length scales may not be practical. Additionally, the presence of inert materials (which are generally greater than 75% by mass) implies an increase in the sensible heat required to drive the reduction, which in turn decreases $\eta_{\text{solar-to-fuel}}$.

Ferrites

Substitution of transition metal ions for iron in the magnetite lattice (i.e. $\text{M} = \text{Ni}$ and Co in $\text{M}_x\text{Fe}_{3-x}\text{O}_4$) can increase oxygen storage capacity compared to pure magnetite. As the concentration of the substituted transition metal increases in the spinel lattice (x , in $\text{M}_x\text{Fe}_{3-x}\text{O}_4$), the reduction extent at a given temperature and p_{O_2} is increased compared to pure magnetite [24]. This is exemplified in Fig. 2, where predicted equilibrium amounts of oxygen evolved from $\text{Co}_x\text{Fe}_{3-x}\text{O}_4$ at 1473 K are shown for various degrees of cobalt substitution and p_{O_2} 's. Data are shown for relatively large reduction extents where only nonstoichiometric cobalto-wüstite is stable ($(\text{Co}_y\text{Fe}_{1-y})_{1-\delta}\text{O}$, where $y = x/3$) because thermodynamic data for this system is well documented [44], and as seen, reduction extents clearly increase with increasing cobalt concentration for a given p_{O_2} . For lower reduction extents, solid solutions of magnetite–wüstite phases are thermodynamically predicted [45].

Although reduction extents are increased with cobalt content, the resulting thermodynamic potential for oxidation is decreased,

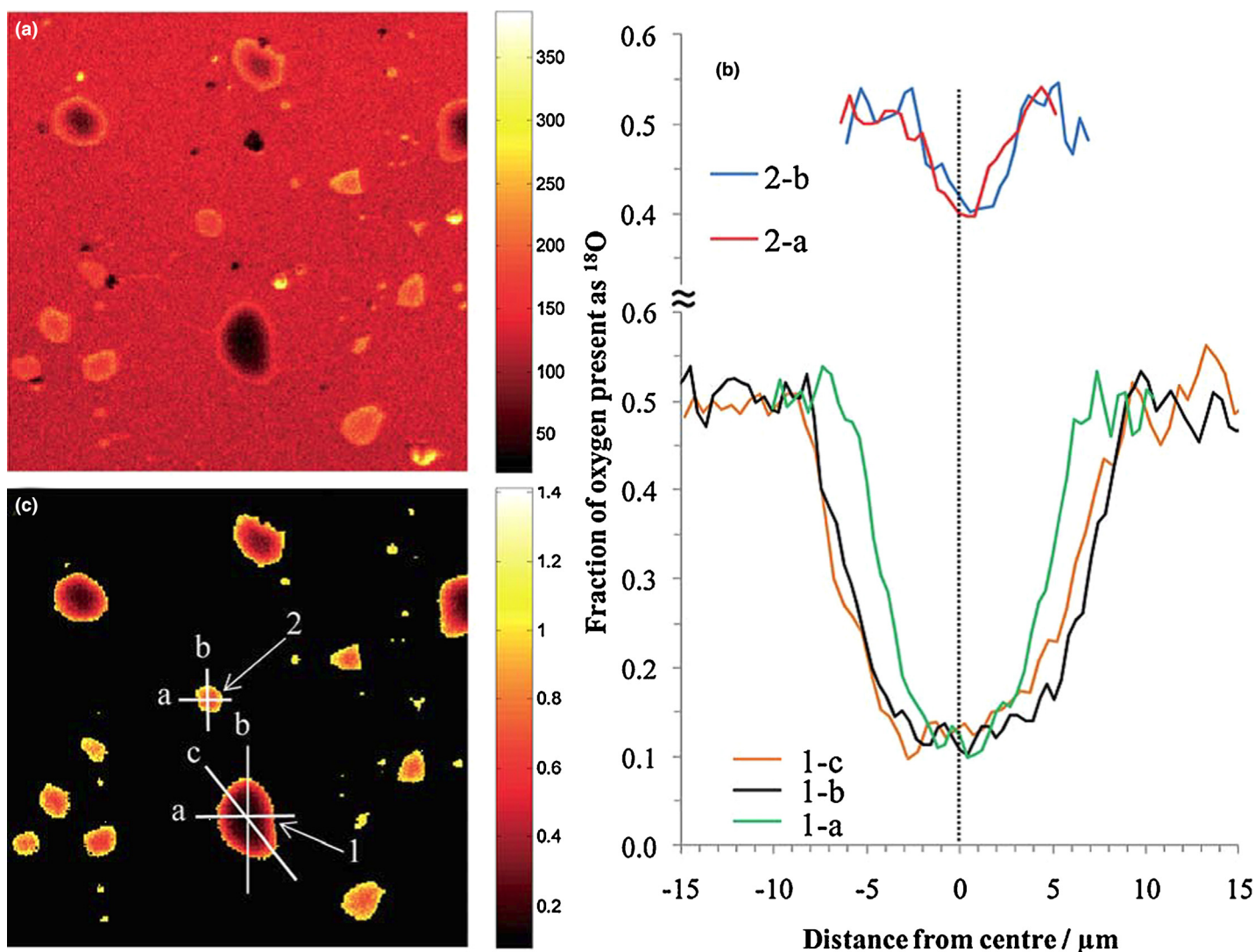


FIGURE 1

Raw ToF-SIMS image of ^{18}O intensity (a) and masked $^{18}\text{O}/^{16}\text{O}$ ratio intensity (b) for 14.5 mol% Fe in 8YSZ. The image area is $100 \mu\text{m} \times 100 \mu\text{m}$. Line-scans of $^{18}\text{O}/(^{16}\text{O} + ^{18}\text{O})$ intensity for particles 1 and 2 (c). Scan lines are defined in (b). The vertical dotted line defines the center of the particles. Graphic reproduced with permission from Coker et al. [42].

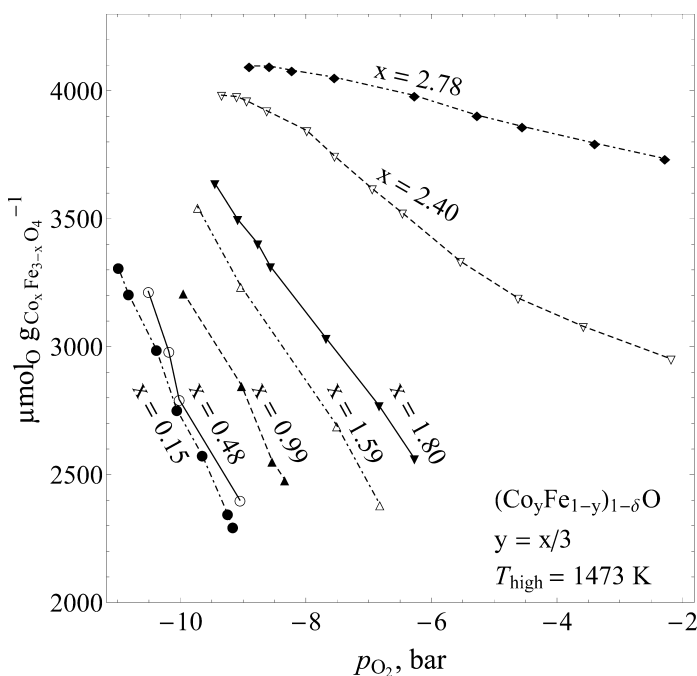
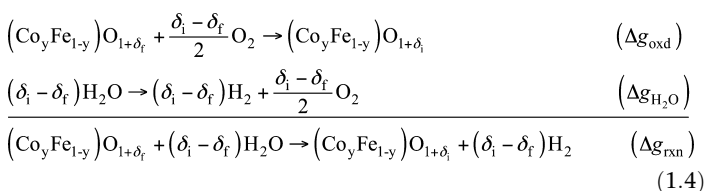


FIGURE 2

Gaseous equilibrium oxygen yields resulting from the reduction of $\text{Co}_x\text{Fe}_{3-x}\text{O}_4$ to $(\text{Co}_y\text{Fe}_{1-y})_{1-\delta}\text{O}$, where $y = x/3$. Data extracted from Ref. [44].

and in the extreme case of complete substitution of $\text{Co}^{3+/2+}$ for $\text{Fe}^{3+/2+}$ (Co_3O_4), the resulting reduced oxide (CoO) is not capable of being reoxidized with water or carbon dioxide [8]. Thus, oxygen storage capacity is not necessarily increased because reduction extents are greater. Allendorf et al. performed a systematic thermodynamic study of various ferrite compositions and concluded that both $\text{Ni}_x\text{Fe}_{3-x}\text{O}_4$ and $\text{Co}_x\text{Fe}_{3-x}\text{O}_4$, where $x = 1$, are preferable for maximizing oxygen storage capacity and thus fuel yields [24]. However, it was reported that compared to a purely iron system, care must be taken to ensure that stable intermediate phases are not formed during redox reactions, especially when $x > 1$ or $x < 1$.

The oxidation potential with H_2O or CO_2 as a function of cobalt concentration can be realized through knowledge of the partial molar free energy of oxygen (Δg_{O}) in the region where nonstoichiometric cobalto-wustite is stable. The oxidation of $(\text{Co}_y\text{Fe}_{1-y})_{1-\delta}\text{O}$ with H_2O , for example, can be described by the sum of the following reactions (typically, cobalto-wustites are designated as $(\text{Co}_y\text{Fe}_{1-y})_{1-\delta}\text{O}$ to indicate that cation vacancies are the predominant defect. For simplification purposes, we use instead $(\text{Co}_y\text{Fe}_{1-y})\text{O}_{1-\delta}$ to show how O moles change during reaction):



$\Delta g_{\text{H}_2\text{O}}$ is the free energy of water dissociation, Δg_{rxn} is the free energy of the oxide oxidation with H_2O , and Δg_{oxd} is the free

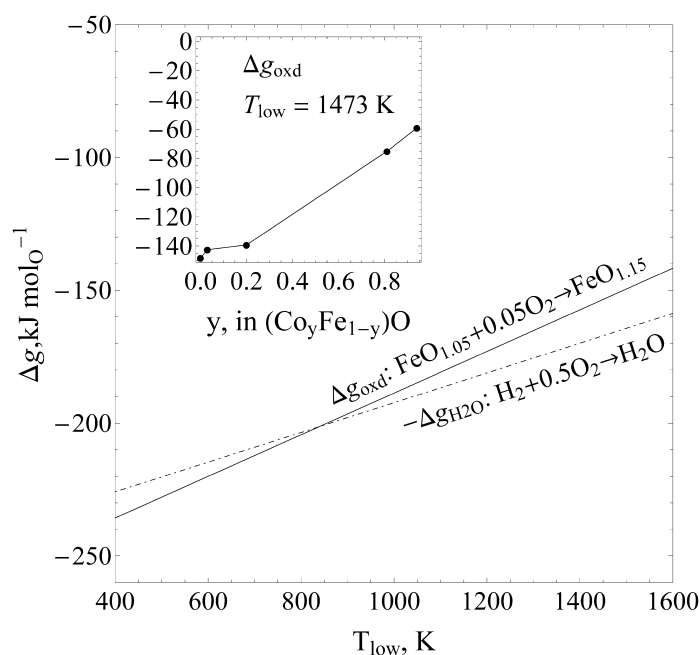


FIGURE 3

Δg_{oxd} and $\Delta g_{\text{H}_2\text{O}}$ versus temperature for the wustite system, derived from thermodynamic data from Nowotny and Rekas [40]. Shown in the inset is the effect of increasing cobalt concentration on Δg_{oxd} (only at 1473 K), derived from thermodynamic data presented in Ref. [47].

energy of oxide oxidation with O_2 and is related to the Δg_{O} through the following relationship [46]:

$$\Delta g_{\text{oxd}} = \frac{\int_{\delta_f}^{\delta_i} \Delta g_{\text{O}} d\delta}{\delta_i - \delta_f} \quad (1.5)$$

Thus, according to Eqn. (1.4), oxidation is thermodynamically favorable when $\Delta g_{\text{oxd}} < -\Delta g_{\text{H}_2\text{O}}$. Δg_{O} for cobalto-wustites has been determined from equilibrium data as described by Raeder et al., but only at 1473 K [47]. More complete partial thermodynamic (Δh_{O} and Δs_{O}) properties are documented for nonstoichiometric wustite that allow one to solve for Δg_{O} as a function of temperature ($\Delta g_{\text{O}} = \Delta h_{\text{O}} + T\Delta s_{\text{O}}$) [40]. Shown in Fig. 3 is Δg_{oxd} and $-\Delta g_{\text{H}_2\text{O}}$ (H_2O thermodynamic properties determined from the NIST-JANAF thermochemical tables) versus temperature for a purely iron system and as seen Δg_{oxd} is lower than $-\Delta g_{\text{H}_2\text{O}}$ at low temperatures ($T < 850$ K), indicating that Δg_{rxn} is thermodynamically favorable below this temperature. The negative effect of increasing cobalt content on Δg_{oxd} (and thus Δg_{rxn}) can be seen in the inset of Fig. 3. Results are qualitatively consistent with predictions from thermodynamic models that show that oxidation extents are minimal for large cobalt concentrations [8,24].

Similarly to magnetite, ferrites are usually stabilized with or dissolved in inert materials to prevent sintering and melting. Kodama et al. experimentally demonstrated Ni and Co ferrite based redox cycles when mixing with YSZ or ZrO_2 [22,48]. H_2 yields were greater on a per mass basis compared to Fe-YSZ systems, qualitatively supporting the thermodynamic modeling performed by Allendorf et al. [24]. Scheffe et al. has performed a kinetic analysis of the water oxidation step over thermally reduced $\text{Co}_{0.9}\text{Fe}_{2.1}\text{O}_4/\text{ZrO}_2$ composite samples [23] and their results further

support the C(^{18}O) $_2$ isotopic study performed by Coker et al. [42]. The analysis indicated that two simultaneous reactions are occurring, namely (1) oxidation of Fe^{2+} dissolved in the ZrO_2 lattice and (2) oxidation of Fe^{2+} within a cobalt ferrite solid solution.

Hercynite

The thermodynamic barrier for reduction is decreased when iron oxide based materials are reduced in the presence of Al_2O_3 . Reduction of Fe^{3+} to Fe^{2+} proceeds via the formation of an iron aluminate and substitute metal aluminate ($\text{M}_x\text{Fe}_{3-x}\text{O}_4 + 3\text{Al}_2\text{O}_3 \rightarrow (3-x)\text{FeAl}_2\text{O}_4 + x\text{MAl}_2\text{O}_4$)²⁵ and upon re-oxidation the ferrite and alumina are reformed. The so-called “hercynite cycle” was demonstrated by Scheffe et al. who showed that H_2 yields of $\text{CoFe}_2\text{O}_4/\text{Al}_2\text{O}_3$ reduced at 1473 K approach $600 \mu\text{mol g}_{\text{ferrite}}^{-1}$, which is roughly 4 times greater than CoFe_2O_4 [25]. At 1673 K, however, H_2 yields of CoFe_2O_4 are greater. The results are in qualitative agreement with thermodynamic predictions. Arifin et al. have demonstrated the cycle using CoFe_2O_4 deposited via atomic layer deposition (ALD) on high surface area Al_2O_3 structures [26]. They show that the reaction kinetics are rapid compared to bulk iron oxide structures, likely due to the small length scales of the ALD films. More recently, Muhich et al. demonstrated the cycle isothermally, where reduction and oxidation are driven by changes in oxygen activity rather than temperature swings [27]. They show that for isothermal water splitting at 1523 K, H_2 yields are >3 times the traditional hercynite cycle and >12 times the ceria cycle (to be discussed) when they are cycled between 1523 K and 1273 K. The increase in yields was primarily attributed to increases of local oxygen activity near the reactive surface, allowing the oxidation reaction to proceed further than when only changing temperature. Several other researchers have recently demonstrated the advantages of isothermal redox cycling [49,50]. Specifically, thermal and mechanical stresses are less of a concern because rapid temperature changes are not necessary. Additionally, sensible heat recuperation from the gas phase (a relatively mature technologically) dominates process efficiencies rather than heat recuperation from the solid phase [50].

Ceria

In 2006 Abanades and Flamant demonstrated a redox cycle based on the stoichiometric reduction of CeO_2 to Ce_2O_3 [51]. Reduction was conducted at 2273 K, below the melting point of ceria, but extensive sublimation was observed (>50%) [51]. Following these results, Chueh and Haile proposed a similar cycle based on the nonstoichiometric reduction of ceria ($\text{CeO}_2 \rightarrow \text{CeO}_{2-\delta}$) which does not require the extreme temperatures necessary for stoichiometric reduction [52]. Several researchers have demonstrated this cycle, and in 2010, Chueh et al. developed and tested the first ceria-based solar reactor, successfully demonstrating the viability of the cycle under realistic solar concentrating conditions [53]. The simultaneous splitting of H_2O and CO_2 was experimentally shown in 10 consecutive cycles, yielding syngas with a $\text{H}_2:\text{CO}$ molar ratio that can be controlled by adjusting the $\text{H}_2\text{O}:\text{CO}_2$ molar ratio in the reacting gas [54]. Panlener et al. [55] and Toft Sorenson [46] have studied the oxygen nonstoichiometry and defect chemistry of nonstoichiometric ceria at elevated temperatures, and while the oxygen exchange capability of ceria is lower compared to iron

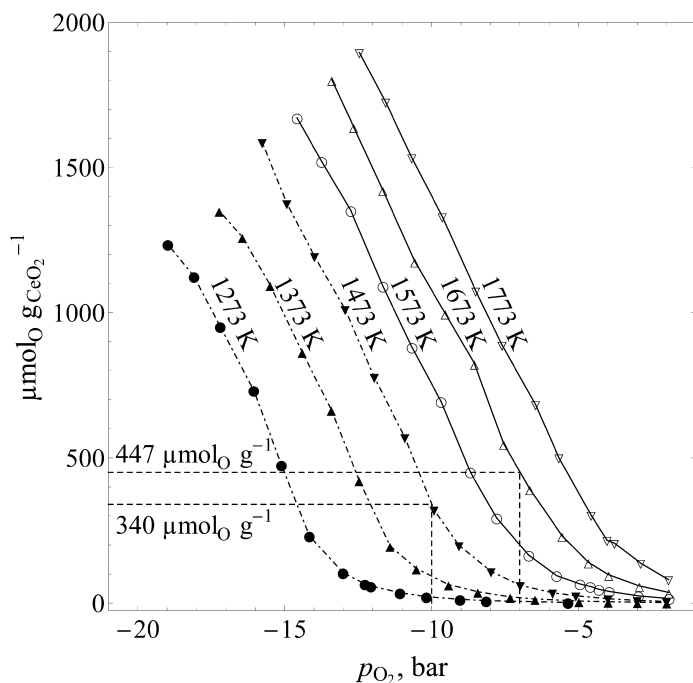


FIGURE 4

Gaseous equilibrium oxygen yields as a function of temperature and p_{O_2} resulting from the reduction of CeO_2 to $\text{CeO}_{2-\delta}$. Data extracted from Ref. [55].

oxide based cycles, sintering is less problematic because the melting point is considerably higher [56]. Thus, it is not necessary to support or dissolve them within more stable structures. Electronic and ionic conductivities of pure ceria, which directly dictate ambipolar oxygen diffusion rates, are also well documented [57,58]. Diffusion of oxygen is orders of magnitude faster than diffusion of Fe^{2+} in iron oxide and ferrites [58,59], rendering larger length scales (l) suitable for driving redox reactions. This was demonstrated in a solar reactor using a ceria reticulated porous ceramic ($l \approx 1 \text{ mm}$) by Furler et al. [28]. $\eta_{\text{solar-to-fuel}}$ was 1.73% average and 3.53% peak; which is roughly 4 times greater than the next highest reported values to date for a solar-driven device. Reaction extents during reduction were shown to be limited by heat transfer rather than chemical diffusion of oxygen or surface kinetic limitations. Oxidation rates with CO_2 were dependent on specific surface area ($\approx 30 \text{ min}$ at 900°C), but were shown to be considerably faster than iron oxide based materials of much smaller length scales [28,42]. Cyclical stability has been examined by Chueh and Haile [13], yielding a noticeable drop in yields and oxidation rates during the first 100 cycles due to sintering and grain growth, followed by 400 cycles with remarkable stability of H_2/O_2 yields and H_2 rates.

While ceria is attractive from a kinetic and stability perspective, its oxygen storage capacity suffers compared to most other redox materials. See Fig. 4, for example, where equilibrium oxygen yields resulting from the reduction of CeO_2 are shown versus temperature and p_{O_2} , extracted from thermodynamic data of Panlener et al. [55]. Reduction yields are roughly 1/8 of cobalt ferrite ($x = 0.15$) discussed in Fig. 2, at $T = 1473$, $p_{\text{O}_2} = 10^{-10}$ bar. As a result, for this cycle to achieve a high $\eta_{\text{solar-to-fuel}}$, and thus become economically feasible, efficient heat recuperation from either the solid or gas phases are absolutely necessary [58].

Doped ceria

The thermodynamic and kinetic properties of ceria can be altered by doping its fluorite structure with transition metal and rare earth metal oxides. Dopants considered for ceria-based cycles include +2 (Ca, Sr, Li) [32,60–62], +3 (Sm, Gd, Y, Cr, Pr, La, Sc) [32,52,61–64] and +4 (Zr, Hf) [31,32,61,64–66] cations. The introduction of +2 and +3 dopants result in stable intrinsic oxygen vacancies [67,68], and thus an increase in electronic mobilities within the ceria lattice [69]. Because diffusion of oxygen in ceria occurs via ambipolar diffusion of both electrons and ions, the introduction of intrinsic vacancies results in higher oxygen diffusion coefficients compared to pure ceria [13]. Le Gal and Abanades introduced La^{3+} , Y^{3+} , Pr^{3+} and Gd^{3+} into Zr-doped ceria and report that oxidation rates are faster because of decreased diffusion limitations. Moreover, the addition of La^{3+} was shown to improve the thermal stability upon repetitive cycling [65]. However, +2 and +3 dopants have not been shown to increase reduction extents compared to pure ceria (at conditions relevant to thermochemical cycles, high T_{high} and p_{O_2}), and thus their introduction is not expected to have a thermodynamic benefit [32,62].

Tetravalent dopants have been shown to have a positive effect on increasing reduction extents under conditions relevant to thermochemical cycles. Le Gal et al. [31] report that gravimetric amounts of oxygen evolved for Zr-doped ceria level off at nearly 25 mol% Zr, but that the absolute amount of cerium ions reduced increases with Zr^{4+} concentrations up to 54 mol%. These results are in good agreement with Call et al. [66] and thermodynamic data reported by Kuhn et al. [14] and Shah et al. [70] who show that the reducibility of Ce^{4+} is increased with the introduction of Zr^{4+} dopants (<20 mol%) due to a decrease in the partial oxygen molar enthalpy. Kuhn et al. report Δh_{O} values ranging between -364 and

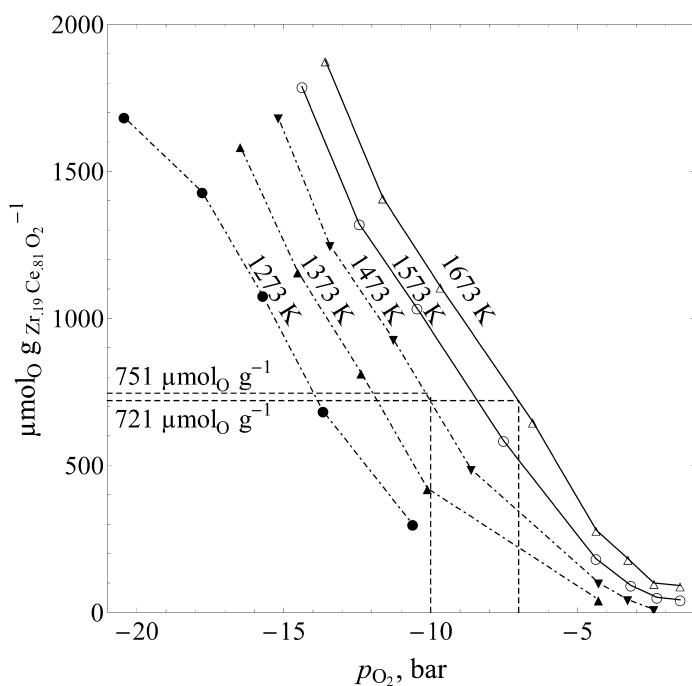


FIGURE 5

Gaseous equilibrium oxygen yields as a function of temperature and p_{O_2} resulting from the reduction of $\text{Zr}_{0.19}\text{Ce}_{0.81}\text{O}_2$ to $\text{Zr}_{0.19}\text{Ce}_{0.81}\text{O}_{2-\delta}$. Data extracted from Ref. [71].

-250 kJ mol^{-1} with a minimum near 50 mol% Zr^{4+} , while Shah et al. report similar values for Zr^{4+} concentrations of 25 and 75 mol% (-290 to -250 kJ mol^{-1}). As reduction extents increase to $\delta = 0.075$, partial molar enthalpies linearly decrease, but for larger reduction extents they are roughly constant. Δh_{O} for ceria, on the other hand, are considerably larger and range from -480 to -384 kJ mol^{-1} as δ increases from 0 to 0.15 [55]. Meng et al. have also shown improvement in reduction yields when doping with 10 mol% Hf^{4+} and doping of $\text{Hf}^{4+}/\text{Pr}^{3+}$ [32,61]. However, sufficient thermodynamic data of hafnia–ceria systems is lacking for a direct comparison to the zirconia–ceria system. Nonstoichiometry of 19 mol% Zr-doped ceria has been measured at elevated temperatures by Hao et al. [71]. Results are summarized in Fig. 5, where δ in $\text{Ce}_{0.81}\text{Zr}_{0.19}\text{O}_{2-\delta}$ (translated to mol O g^{-1}) is shown as a function of T and p_{O_2} . As seen, reduction extents for Zr-doped ceria are greater than pure ceria under all conditions considered. For example, at $p_{\text{O}_2} = 10^{-7}$ bar and $T = 1673 \text{ K}$, expected reduction extents for 19 mol% Zr-doped ceria are 721 mol O g^{-1} compared to 447 mol O g^{-1} for pure ceria. Extrapolating the results from Fig. 2, both pure and Zr-doped ceria systems are expected to reduce less than iron oxide based systems. Yet, it cannot be overlooked that iron oxide materials are usually supported within inert stabilizer, effectively lowering their reduction yields on a basis of total mass.

Similar to the effect of increasing Co concentrations in $\text{Co}_x\text{Fe}_{3-x}\text{O}_4$, oxidation thermodynamics of Zr-doped systems are not as favorable as pure ceria. Following the methodology described in Eqns. (1.4) and (1.5), and applying partial molar thermodynamic properties reported by Kuhn et al. [14], Δg_{oxd} values are shown versus temperature for various Zr^{4+} concentrations and compared to $-\Delta g_{\text{H}_2\text{O}}$ in Fig. 6. As seen, Δg_{oxd} of reduced ceria is lower than both 5 and 20 mol% Zr^{4+} for all temperatures, and lower than

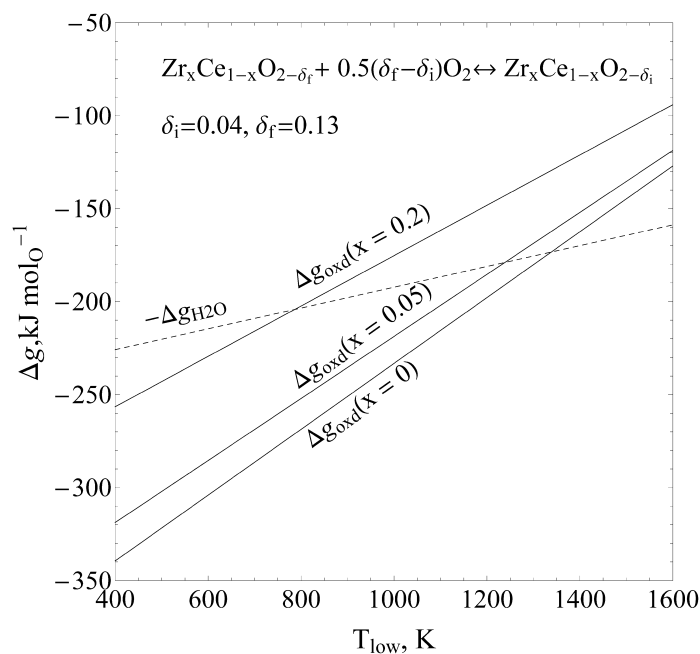


FIGURE 6

Δg_{oxd} and $\Delta g_{\text{H}_2\text{O}}$ versus temperature for various degrees of Zr concentrations in $\text{Zr}_x\text{Ce}_{1-x}\text{O}_{2-\delta}$, derived from thermodynamic data from Kuhn et al. [14].

$-\Delta g_{\text{H}_2\text{O}}$ until roughly 1300 K. On the other hand, 20 mol% Zr-doped ceria is lower than $-\Delta g_{\text{H}_2\text{O}}$ only below 800 K. Several reports have indicated that oxidation of Zr-doped systems is more difficult than pure ceria, but it is not clear if this is purely a thermodynamic phenomenon and or also related to kinetic limitations [30,65].

Perovskites

Perovskites of the form $\text{ABO}_{3-\delta}$ remain a class of nonstoichiometric oxides that are widely unexplored for thermochemical cycles. Dopants can be substituted on both A and B cation sites, and thus the number of potential material configurations is substantially greater than ceria based systems. A thermodynamic analysis based on evaluation of oxygen nonstoichiometry data and extraction of partial enthalpies and entropies by Scheffe et al. has shown that LSM perovskites ($\text{La}_{1-x}\text{Sr}_x\text{MnO}_{3-\delta}$) can increase oxygen exchange capacity compared to pure ceria [34]. Experiments indicated that reduction extents are considerably greater (≈ 2 times by mass at $T_{\text{high}} = 1773$ K), but oxidation thermodynamics are less favorable, resulting in incomplete oxidation. Nevertheless total CO yields during CO_2 splitting cycles are still substantially greater than ceria. An even more promising class of perovskites was explored by McDaniel et al. [33]. By doping $\text{LaAlO}_{3-\delta}$ perovskites with $\text{Mn}^{2+/3+/4+}$ on B sites and Sr^{2+} on A sites, so called SLMA perovskites, they were able to increase H_2 yields by $9\times$ and CO yields by $6\times$ compared to ceria when reduced at 1523 K and oxidized at 1273 K. Shown in Fig. 7 is an exemplary plot of the temporal oxidation behavior of three different SLMA

perovskites (see figure caption for exact compositions) compared to pure ceria. Remarkably, reaction kinetics are shown to be similar to ceria and stability has been demonstrated for up to 80 redox cycles, in contrast to ferrite based systems. Evdou et al. have studied $\text{La}_{1-x}\text{Sr}_x\text{FeO}_{3-\delta}$ for chemical looping applications [72]. CH_4 is used during reduction, resulting in lower temperatures (1000–1273 K) than a thermally driven process, and synthesis gas is simultaneously generated. Maximum H_2 yields are achieved using $\text{La}_{0.3}\text{Sr}_{0.7}\text{FeO}_{3-\delta}$ mixed with 5% NiO. These results show the potential promise of perovskite based systems, and based on the number of doping schemes which one could consider, a number of even more attractive materials certainly remain to be discovered.

Conclusions

The ultimate factor dictating commercial viability of solar thermochemical fuel production is a high solar-to-fuel energy conversion efficiency [73]. Discovery of new materials with large oxygen exchange capabilities at moderate temperatures and their implementation in efficient solar reactors are essential. Thermodynamic analysis based on either first principle calculations [74] or empirical data (i.e. ternary or quaternary perovskite systems), for example, can provide insights into material screening. Additionally, rapid chemical kinetics and material stability over thousands of cycles must be demonstrated for each material considered. Ultimately, design and testing of prototype solar reactors and optimization through heat and mass transfer modeling will lead to improvements in solar-to-fuel energy conversion efficiencies.

Acknowledgements

Financial support by the Swiss Competence Center Energy & Mobility, the Swiss Federal Office of Energy, the Helmholtz-Gemeinschaft Deutscher Forschungszentren (Virtuelles Institut SolarSyngas), and the European Research Council under the European Union's ERC Advanced Grant (SUNFUELS-Nr. 320541) is gratefully acknowledged.

References

- [1] E.A. Fletcher, R.L. Moen, *Science* 197 (4308) (1977) 1050–1056.
- [2] T. Riedel, G. Schaub, *Top. Catal.* 26 (1–4) (2003) 145–156.
- [3] S. Ihara, *Int. J. Hydrogen Energy* 3 (3) (1978) 287–296.
- [4] T. Nakamura, *Solar Energy* 19 (5) (1977) 467–475.
- [5] Y. Nigara, B. Gales, *Bull. Chem. Soc. Jpn.* 59 (6) (1986) 1997–2002.
- [6] A. Steinfeld, *Solar Energy* 78 (5) (2005) 603–615.
- [7] G.P. Smestad, A. Steinfeld, *Ind. Eng. Chem. Res.* 51 (37) (2012) 11828–11840.
- [8] T. Kodama, N. Gokon, *Chem. Rev.* 107 (10) (2007) 4048–4077.
- [9] TIAx Support for Cost Analyses on Solar-driven High Temperature Thermochemical Water-splitting Cycles, U.S. Department of Energy, 2011. p. 76.
- [10] R. Perret, *Solar Thermochemical Hydrogen Production Research (STCH)*, Sandia National Laboratories Report, 2011, pp. 1–117 SAND2011-3622.
- [11] A. Steinfeld, *Int. J. Hydrogen Energy* 27 (6) (2002) 611–619.
- [12] I. Alxneit, *Solar Energy* 82 (11) (2008) 959–964.
- [13] W.C. Chueh, S.M. Haile, *Philos. Trans. R. Soc. A: Math. Phys. Eng. Sci.* 368 (1923) (2010) 3269–3294.
- [14] M. Kuhn, et al. *Acta Mater.* 61 (11) (2013) 4277–4288.
- [15] C. Perkins, P.R. Lichty, A.W. Weimer, *Int. J. Hydrogen Energy* 33 (2) (2008) 499–510.
- [16] P.G. Loutzenhiser, A. Meier, A. Steinfeld, *Materials* 3 (11) (2010) 4922–4938.
- [17] S. Abanades, et al. *Int. J. Hydrogen Energy* 33 (21) (2008) 6021–6030.
- [18] E.N. Coker, et al. *J. Mater. Chem.* 21 (29) (2011) 10767–10776.
- [19] P. Charvin, et al. *Energy* 32 (7) (2007) 1124–1133.
- [20] T. Kodama, Y. Nakamuro, T. Mizuno, *J. Solar Energy Eng.* 128 (1) (2006) 3–7.
- [21] N. Gokon, et al. *Int. J. Hydrogen Energy* 34 (3) (2009) 1208–1217.
- [22] T. Kodama, et al. *Solar Energy* 78 (5) (2005) 623–631.

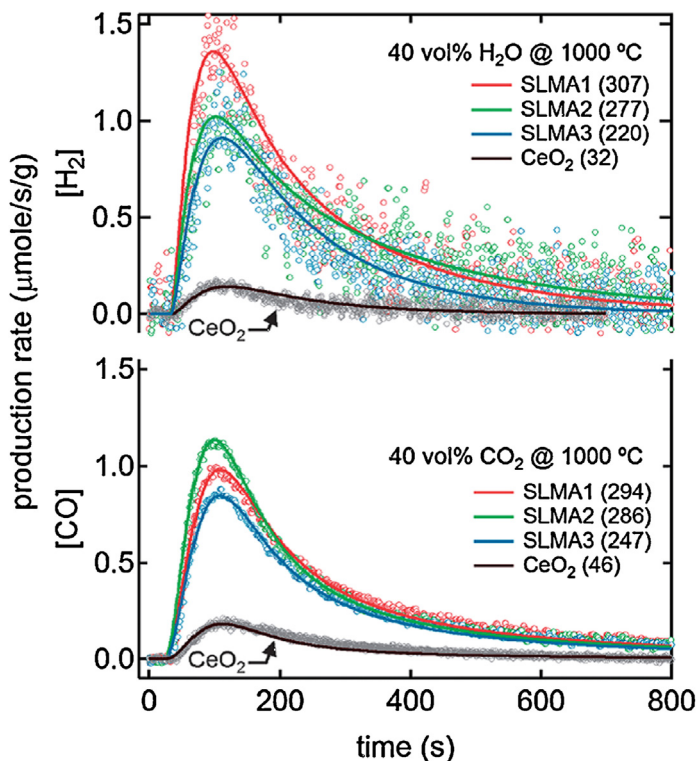


FIGURE 7

(Top) H_2 and (bottom) CO production rates as a function of time for three different SLMA perovskites reduced at 1523 K in He. Parentheses indicate total yields in $\mu\text{mol/g}$ material. SLMA1 = $\text{Sr}_{0.6}\text{La}_{0.4}\text{Mn}_{0.6}\text{Al}_{0.4}\text{O}_{3-\delta}$, SLMA2 = $\text{Sr}_{0.4}\text{La}_{0.6}\text{Mn}_{0.6}\text{Al}_{0.4}\text{O}_{3-\delta}$, SLMA3 = $\text{Sr}_{0.4}\text{La}_{0.6}\text{Mn}_{0.4}\text{Al}_{0.6}\text{O}_{3-\delta}$. Reproduced with permission from McDaniel et al. [33].

- [23] J.R. Scheffe, et al. *Energy Environ. Sci.* 6 (3) (2013) 963–973.
- [24] M.D. Allendorf, et al. *Energy Fuels* 22 (6) (2008) 4115–4124.
- [25] J.R. Scheffe, J. Li, A.W. Weimer, *Int. J. Hydrogen Energy* 35 (8) (2010) 3333–3340.
- [26] D. Arifin, et al. *Energy Environ. Sci.* 5 (11) (2012) 9438–9443.
- [27] C.L. Muhich, et al. *Science* 341 (6145) (2013) 540–542.
- [28] P. Furler, et al. *Energy Fuels* 26 (2012) 7051–7059.
- [29] Y. Hao, C.-K. Yang, S.M. Haile, *Phys. Chem. Chem. Phys.* 15 (2013) 17084–17092.
- [30] S. Abanades, et al. *J. Mater. Sci.* 45 (15) (2010) 4163–4173.
- [31] A. Le Gal, et al. *Energy Fuels* 27 (2013) 6068–6078.
- [32] Q.-L. Meng, et al. *Int. J. Hydrogen Energy* 36 (21) (2011) 13435–13441.
- [33] A.H. McDaniel, et al. *Energy Environ. Sci.* 6 (8) (2013) 2424–2428.
- [34] J.R. Scheffe, D. Weibel, A. Steinfeld, *Energy Fuels* 27 (8) (2013) 4250–4257.
- [35] A. Steinfeld, S. Sanders, R. Palumbo, *Solar Energy* 65 (1) (1999) 43–53.
- [36] I. Bransky, A.Z. Hed, *J. Am. Ceram. Soc.* 51 (4) (1968) 231.
- [37] L.S. Darken, R.W. Gurry, *J. Am. Chem. Soc.* 67 (8) (1945) 1398–1412.
- [38] O.N. Salmon, *J. Phys. Chem.* 65 (3) (1961) 550–556.
- [39] L.S. Darken, R.W. Gurry, *J. Am. Chem. Soc.* 68 (5) (1946) 798–816.
- [40] J. Nowotny, M. Rekas, *J. Am. Ceram. Soc.* 72 (7) (1989) 1221–1228.
- [41] R. Dieckmann, *Ber. Bunsen. Phys. Chem.* 86 (2) (1982) 112–118.
- [42] E.N. Coker, et al. *J. Mater. Chem.* 22 (14) (2012) 6726–6732.
- [43] J.R. Scheffe, et al. *Chem. Mater.* 23 (8) (2011) 2030–2038.
- [44] W.-W. Zhang, M. Chen, *Calphad* 41 (2013) 76–88.
- [45] R. Subramanian, R. Dieckmann, *J. Phys. Chem. Solids* 55 (1) (1994) 59–67.
- [46] O. Toft Sorenson, *J. Solid State Chem.* 18 (3) (1976) 217–233.
- [47] J.H. Raeder, J.L. Holm, O.T. Sørensen, *Solid State Ionics* 12 (1984) 155–159.
- [48] T. Kodama, N. Gokon, R. Yamamoto, *Solar Energy* 82 (1) (2008) 73–79.
- [49] Y. Hao, C.-K. Yang, S.M. Haile, *Phys. Chem. Chem. Phys.* 15 (40) (2013) 17084–17092.
- [50] R. Bader, et al. *Energy Fuels* 27 (9) (2013) 5533–5544.
- [51] S. Abanades, G. Flamant, *Solar Energy* 80 (12) (2006) 1611–1623.
- [52] W.C. Chueh, S.M. Haile, *ChemSusChem* 2 (8) (2009) 735–739.
- [53] W.C. Chueh, et al. *Science* 330 (6012) (2010) 1797–1801.
- [54] P. Furler, J.R. Scheffe, A. Steinfeld, *Energy Environ. Sci.* 5 (3) (2012) 6098–6103.
- [55] R.J. Panlener, R.N. Blumenthal, J.E. Garnier, *J. Phys. Chem. Solids* 36 (11) (1975) 1213–1222.
- [56] M. Mogensen, N.M. Sammes, G.A. Tompsett, *Solid State Ionics* 129 (1–4) (2000) 63–94.
- [57] M.A. Panhans, R.N. Blumenthal, *Solid State Ionics* 60 (4) (1993) 279–298.
- [58] G.J. VanHandel, R.N. Blumenthal, *J. Electrochem. Soc.* 121 (9) (1974) 1198–1202.
- [59] R. Dieckmann, H. Schmalzried, *Ber. Bunsen. Phys. Chem.* 81 (3) (1977) 344–347.
- [60] Q.-L. Meng, et al. *J. Solid State Chem.* 194 (2012) 343–351.
- [61] Q.-L. Meng, Y. Tamaura, *J. Phys. Chem. Solids* 75 (2014) 328–333.
- [62] J.R. Scheffe, A. Steinfeld, *Energy Fuels* 26 (3) (2012) 1928–1936.
- [63] P. Singh, M.S. Hegde, *Chem. Mater.* 22 (3) (2009) 762–768.
- [64] J.R. Scheffe, et al. *J. Phys. Chem. C* 117 (2013) 24104–24114.
- [65] A. Le Gal, S. Abanades, *J. Phys. Chem. C* 116 (25) (2012) 13516–13523.
- [66] F. Call, et al. *Am. J. Anal. Chem.* 4 (10A) (2013) 37–45.
- [67] L. Gauckler, M. Gödickemeier, D. Schneider, *J. Electroceram.* 1 (2) (1997) 165–172.
- [68] T. Kobayashi, et al. *Solid State Ionics* 126 (3/4) (1999) 349–357.
- [69] S. Wang, et al. *J. Electrochem. Soc.* 147 (10) (2000) 3606–3609.
- [70] P.R. Shah, et al. *Chem. Mater.* 18 (22) (2006) 5363–5369.
- [71] Y. Hao, W.C. Chueh, S.M. Haile, ECS, vol. MA2012-02, ECS, Honolulu, Hawaii, 2012, , Abstract 1823.
- [72] A. Evdou, V. Zaspalis, L. Nalbandian, *Fuel* 89 (6) (2010) 1265–1273.
- [73] N.P. Siegel, et al. *Ind. Eng. Chem. Res.* 52 (9) (2013) 3276–3286.
- [74] B. Meredig, C. Wolverton, *Phys. Rev. B* 80 (24) (2009) 245119.